EFFECT OF FIBRE ORIENTATION ON COMPRESSION MICROMECHANICS IN CFRP INVESTIGATED BY COMPUTED TOMOGRAPHY

Katherine Nelms[1,2]*, Partha P. Paul[1,3], Axel Wowogno[2], Yunhui Chen[1,3,4], Bratislav Lukic[3], Alexander Rack[3], Neha Chandarana[1,2], Philip J. Withers[1]

[1] Henry Royce Institute, Dept. of Materials, University of Manchester, M13 9PL, United Kingdom
katherinejnelms@gmail.com, p.j.withers@manchester.ac.uk
[2] Bristol Composites Institute and Faculty of Engineering, University of Bristol, Bristol, UK
axel.wowogno@bristol.ac.uk, neha.chandarana@bristol.ac.uk
[3] ESRF - The European Synchrotron, Grenoble, 38043 Cédex 9, France
partha.paul@esrf.fr, lukic@esrf.fr, alexander.rack@esrf.fr
[4]School of Engineering, RMIT University, Melbourne, 3000, Australia
yunhui.chen@rmit.edu.au

Keywords: Fibre misalignment, Kink bands, Compression failure, X-ray computed tomography

ABSTRACT

Kink band formation is the primary failure mode of unidirectional carbon fibre reinforced polymer composites (CFRP) loaded under compression, and the kinking stress is highly dependent on defects and fibre misorientation. However, the micromechanics of how defects and fibre misorientation impact kink initiation and propagation is not well understood. In this study, X-ray imaging is used to explore different methods of quantifying fibre misalignment/waviness, manufacturing defects, and their relation to kink band formation. Four samples are characterized; one sample with slightly misoriented fibres is used as a baseline alongside three samples manufactured to have fibres with more sinusoidal (wavy) trajectories. The direction and severity of misalignment is quantified for each fibre, tortuosity is determined and used as a metric for waviness, and voids and resin rich regions are identified. Post-mortem computed tomography is then used to determine the kink plane orientation. The baseline sample kinked in the expected plane, predicted from the sample geometry and notch placement. One sample kinked in a plane parallel to the mean fibre misorientation direction, while kink failure in the final two samples was affected by a combination of voids, resin rich areas, and fibre misalignment.

1 INTRODUCTION

Kink bands are known to be the primary failure mode of unidirectional (UD) fibre reinforced polymer composites (FRPs) loaded under compression [1]–[6] and have been studied extensively since their identification in Rosen's seminal paper in 1965 [4]. The final failure geometry of kink bands has been well characterised from post-mortem sample analysis in 2D [5]–[8] and recently in 3D [9], [10]. It is well accepted that kink bands comprise a region of fibres significantly deflected at an angle from the fibre direction, and which are delineated by parallel planes of fibre fracture. Further, *in situ* studies using optical and SEM microscopy [7], [11]–[13], computed tomography [9], [10], [14], and synchrotron radiography [15], [16], have confirmed long-standing theories that the kinking mechanism is often due to compressive instability giving rise to shear-driven plastic microbuckling matrix failure during loading. This instability can be heightened by buckling-induced delamination which further reduces the lateral constraint to the fibres. The less constrained fibres are free to micro-buckle until reaching a critical point of fracture. The fracture propagates across fibres in the sample, and is typically accompanied by lateral displacement, fibre rotation, and shearing and longitudinal splitting in the matrix.

Currently, there is a lack of understanding of how defects affect kinking micromechanics. Fibre misorientation [2], [17] and voids [18] have both been shown to decrease compression performance. In the case of voids, recent works by Tretiak *et al* [19], [20], have used computed tomography (CT) to characterize the location of voids within composite parts and the impact on fracture propagation during

short beam shear tests. However, to the authors' knowledge, a study has not been conducted mapping misorientation distribution to specific micromechanical events during kink initiation and propagation. Typically, global values for misalignment [2] or their statistical distributions [18] are reported and correlated to a global yield stress.

Quite a few efforts have been made to either develop tools for measuring misalignment or map spatial distribution, a key application being to build high fidelity mechanical models of compression failure. The state of the art currently is to model entire CT volumes [21]. Overall, however, metrics for characterizing fibre misorientation are not yet agreed upon. Initial attempts at characterizing misalignment began with sectioning methods, such as that proposed by Yurgartis [22], but this method was limited by the cumbersome and destructive nature of polishing slices of samples, as well as assumed straight fibres without undulation. Since then, studies have used the term 'misalignment angle' to describe both fibre misalignment from the nominal direction [14], [23] (Figure 1a) and the amplitude of fibre undulation, or waviness, about the direction fibres point [24]–[26] (Figure 1b). Computational methods have been proposed in the last two decades to quantify undulation from slices taken parallel to the fibre direction [24]–[26], but most are still restricted to 2D sections and as such have 180 degree ambiguity.

X-ray CT offers opportunities beyond the 2D limitations of microscopy [27], and is finding increasing application to composite materials [28]. Tomographs are collected by first recording many 2D X-ray images, termed 'projections', or 'radiographs', typically recorded while rotating the sample about one axis. Several hundred radiographs are typically required for a 3D image to be computationally reconstructed. Individual fibre resolution is possible with sufficiently small samples to account for the trade-off between resolution and field of view (FOV) [27]. Several CT studies have applied segmentation methods able to track fibre centres between reconstructed CT slices [29]–[32] and quantify the misalignment of individual fibres [14], [23], [29]. However, to date, few have managed to quantify initial fibre waviness in 3D [30], or assess changes in waviness during loading [14].

The aim of this study is to use CT to characterize the fibre waviness/misalignment and the spatial defect distribution in 3D and to investigate their effect on the kinking micromechanics. To this end a sample (RM) with 'randomly misoriented' straight fibres is used as a baseline alongside three samples (A, B, C) manufactured to have fibres with wavy (sinusoidal) trajectories. The four samples each have a unique spatial distribution of defects and failed in four different orientations. Tomographs collected before compression are used to characterize the resulting spatial distribution of voids and resin rich regions. The InSegt fibre identification package [32] is used to identify individual fibres and calculating misalignment angles from the fibre trajectories. Mean tortuosity [30] for each sample is found as a metric for undulation. Finally, post-mortem tomography is compared against the pre-test tomographs to identify influence of defects and misorientation on the resulting kink plane.

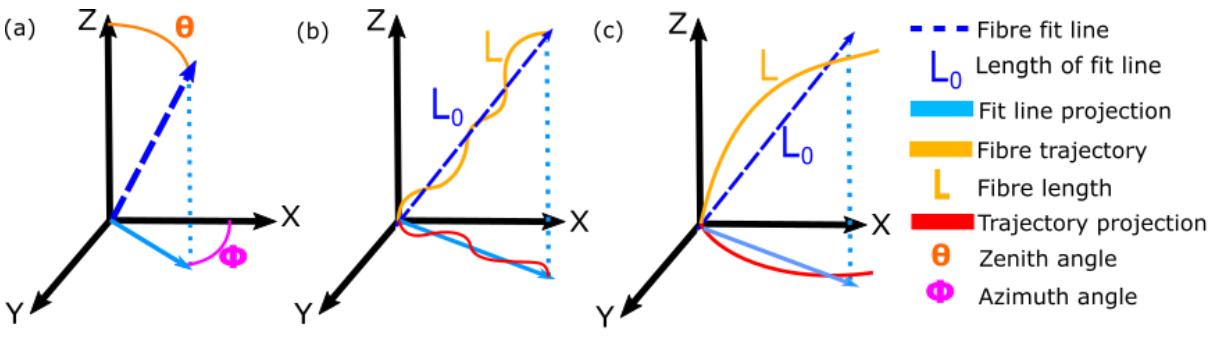

Figure 1: Schematics demonstrating (a) fibre misalignment angles (b) a misaligned fibre with low amplitude, high frequency oscillation (c) a misaligned fibre with similar tortuosity as that in b, but significantly different geometry.

2 EXPERIMENTAL

2.1 Fabricating Samples with Controlled Misorientation

Unidirectional CFRPs were fabricated with deliberate curvature from Cristex ZOLTEK 50K unidirectional non-crimp carbon fibre and infused with Huntsman Araldite LY 564 epoxy resin/Aradur HY 2954 hardener. Six plies of dimensions 10 cm x 10 cm were cut from the dry fibre roll, and the non-crimp fabric (NCF) weft yarns manually removed to minimize the formation of resin rich pockets during infusion. The removal of the weft was essential due to the small sample size required to achieve sub-micron spatial resolution by X-ray imaging. At these length scales of interest (2 mm x 2 mm FOV), the weft yarns perpendicular to the fibre direction cause resin rich regions, which were found to dominate failure in preliminary experiments. Vacuum bagging was specifically chosen over prepreg or small-scale resin infusion [9], [15] to allow for control over the fibre misorientation distribution. Before layup and infusion, a plastic filament of 0.1 mm diameter was placed on the tool plate. Then, the plies were laid up such that the filament was perpendicular to the carbon fibre direction (Figure 2a) to create an out-of-plane waveform relative to the plane of the plies. A second laminate was made using the same vacuum bagging method but without the weft yarn as a baseline for misorientation and undulation. After layup, the plies in both laminates were infused using vacuum-assisted resin infusion before finally being cured at 80°C for eight hours.

After curing, fifteen samples of dimensions 1.5 x 1.5 x 10 mm^3 were cut from each laminate using a Buehler IsoMet 5000 linear precision saw. The long axis was parallel to the primary fibre direction. Finally, the ends of the sample were inserted into steel end caps to better interface with the compression rig and adhered using Araldite® Strength in Bonding epoxy. A notch of 100-150 µm depth was made with a razor blade on the side of each sample, centred to stimulate kink band formation within the FOV of the X-ray detector. For most samples, including those cut from the control laminate, the notch was cut on the side of the sample facing away from the tool plate (Figure 2b). For a third of the wavy samples, the notch was cut on the tool side of the sample to assess whether propagation was different depending on notch placement (Figure 2c).

2.2 Synchrotron Phase-Contrast Tomography

The CT scans were undertaken at the ID19 beamline of the ESRF (Figure 3) [33]. For each sample, tomographs were recorded before and after compression loading. For post-mortem tomography, many of the broken samples did not fit within this window and so tomographs were recorded with the off-centre rotation axis, extending the field of view in horizontal direction. The incident X-rays were a pink (~18keV) beam provided by a first harmonic of the U17 undulator situated 145 m from the sample. For each scan, 6300 radiographs were acquired over a rotation of 360° using a pco.edge 5.5 (PCO GmbH, Germany) camera equipped with microscope lenses (10×/0.3 numerical aperture, Olympus UPLAN) and directly optically coupled to a LSO:Tb (8.7 µm thickness) single-crystal scintillator resulting in a pixel size of 0.65 µm and a field of view of 1.66 x 1.40 mm^2. The detector was set at 70

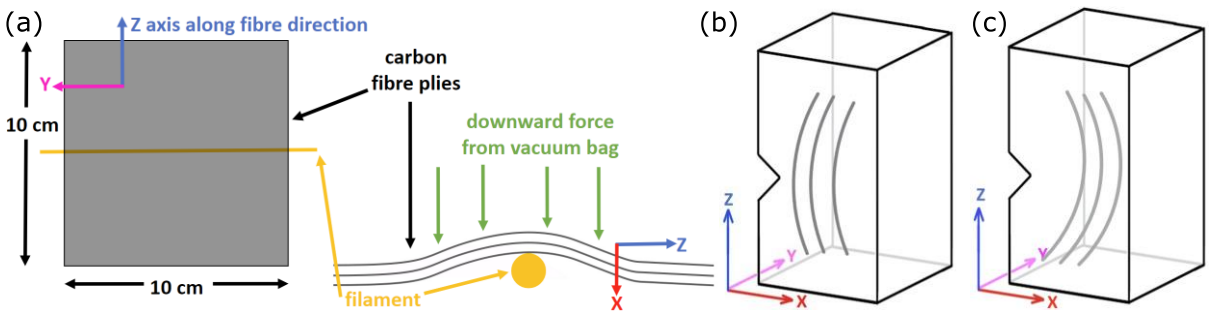

Figure 2: Schematics of (a) layup with weft yarns used to induce undulation (b) sample with notch such that experimental and manufacturing coordinates are the same. (c) sample with notch cut on the 'tool side'. During testing, the y axis was aligned with the X-ray beam.

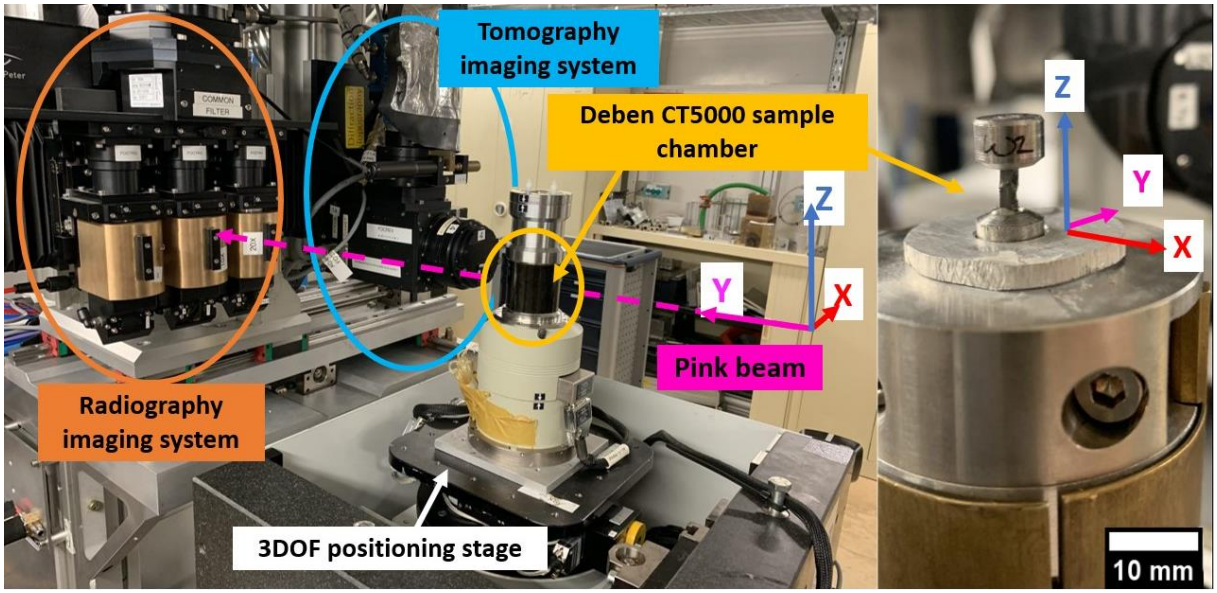

Figure 3: Photograph of ID19 (left) with the Deben rig accommodated on the rotation stage with the radiography detector in place and the tomography detector translated out of the beam (right) magnified image of a composite sample within the lower grip of the Deben straining rig.

mm from the sample, allowing for the propagation-based phase-contrast. After a pre-test CT scan, the samples were compressed at a displacement rate of 0.3 mm/minute using a Deben CT5000 tension-compression rig fitted with a 5kN loadcell. Though the results are not discussed here, during, the test radiographs were collected using an indirect detector used consisting of a Photron FASTCAM SAZ equipped with an objective microscope (10X Mitutoyo Mplan Apo, numerical aperture = 0.28) optically coupled to a LuAG:Ce scintillator (25 µm thickness) via a mirror. The sample stage was not rotated during the compression tests, and the loading was stopped manually once the samples had kinked. Post-mortem tomographs were recorded before unloading to ensure accurate capture of the kinked geometry.

Reconstructions were completed using the Tomwer toolbox and the NABU reconstruction software [34]. The radiographs were first treated using a direct in-line phase retrieval algorithm using the ratio of the real to complex refraction index – $\delta/\beta = 81$ [35]. Then, a Filtered Back Projection algorithm [36] was used to reconstruct the 3D volume. The reconstructed volumes were opened using Avizo 2019 and ImageJ Fiji for 3D visualization.

2.3 Determining Fibre Misalignment Distribution

The majority of the individual fibres were identified for each of the samples using the InSegt fibre analysis scripts for probabilistic segmentation and fibre tracking [32]. This package finds the fibre centres in each slice before matching the centre points between slices to produce a 3D trajectory for each fibre. Before processing, image stacks were adjusted using the 'imadjust' MATLAB command so that each slice had the same contrast. This step was to ensure that the dictionary resulted in a consistent number of centre points detected per slice. To reduce computational time, only every fifth slice of the 2160-image stack was processed, resulting in 432 slices per sample. A threshold of 0.48 was applied to resulting probability maps to produce binarized images. Besides these specifications, default parameters were used for processing to identify fibre centres and generate (x, y, z) coordinates for each fibre. In the case of missed centre-points, the empty (x, y) coordinates were patched with the average of the preceding 5 centre-point coordinates.

The fibre misalignment angles were solved for based on principal component analysis (PCA) [37]. The first principal coordinate was found for the (x, y, z) coordinate array of each tracked fibre using the 'pca' MATLAB command. This unit vector was then used a best fit line by projecting along the length of each fibre to yield the (x, y) coordinates for the fit line corresponding to each z position. The best fit

lines were then used to solve for the azimuth and zenith angles for each fibre; the zenith angle being the angle between the best fit line and the nominal fibre direction (which is taken to be the +Z axis). The zenith angle is bound between 0° and 90°. The azimuth angle is the direction of misorientation, or the angle between the +X axis and the projection of the best-fit line onto the X-Y plane. The azimuth angle is bound between -180° and 180°. Finally, the tortuosity, τ, of each fibre (Figure 1 b and c) for each sample was also calculated from 3D coordinates using the following equation from [30]:

$$\tau = \frac{L}{L_0} - 1 \quad (1)$$

L is the 'real' length of the fibre and is found as the sum of the magnitudes of the relative position vectors between fibre centres in neighbouring slices and L_0 is taken as the end to end length of the fibre. note this is slightly different from the measure defined by Gomaraska *et al*. [30].

3 RESULTS AND DISCUSSION

3.1 Analysis of the As-Manufactured Microstructures

Defects: A CT slice corresponding to the top of the volume for each sample is shown in Figure 4. For all samples, the resin rich areas are located at ply interfaces and where weft yarns were left behind within plies. The three wavy samples have similar spatial distributions of voids concentrated near ply interfaces, suggesting that the filament impacted wetting and resin infusion. In Figure 5, slices at different z-positions within sample B indicating the voids span a significant distance along the z-axis.

Fibre trajectories: Figure 7 (left) shows the projections of the fibre trajectories viewed down the z axis in which a perfectly aligned straight fibre would be represented by a dot, while misaligned, straight fibres shows as a straight line. S' or 'C' shape projections indicate that fibres are both misaligned and wavy. As expected the RM fibres are represented by short, largely straight segments, as are sample B, while the fibres in samples A and C are visibly more misoriented, though the trajectory projections alone cannot inform whether misalignment or waviness is more severe within these samples.

To help distinguish misalignment from waviness, Figure 6b shows that quantitatively, the mean zenith angles for samples A and C (4.46 ± 2.23° and 4.76 ± 1.77°) are approximately 3x that of sample B (1.43 ± 0.90°) and 2x that of RM (2.28 ± 1.71°). For the three wavy samples, the most tortuous fibres are concentrated on the side where the filament was placed, indicated by the severity of the 'C' projections in Figure 7. From Figure 6c, the tortuosity values ranged from 0.1 (fairly wavy) to 0.0001 (minimally wavy), though less than 0.6% of fibres for all samples had a tortuosity smaller than 0.001. Sample A is more tortuous than the other three samples, and the FWHM of the distributions for samples A and B are greater than that of C and RM. The zenith and tortuosity histograms alongside the projections in Figure 7 collectively suggest (1) sample A has highly misaligned and the most tortuous fibres (2) sample B has the best aligned fibres and moderate tortuosity (3) sample C has the most severely misaligned, but relatively straight fibres (4) the RM sample is well aligned and has the straightest fibres.

From Figure 6a, the azimuth angles for fibres in all samples are distributed about 90° and/or -90°, which corresponds to the y-direction within the plane of the laminate (defined in Figure 2). This trend suggests that much of the misorientation is due to the plies not being laid up perfectly parallel, but rather at slight angles to one another. Samples A and C are most severely misaligned (Figure 6b), but largely in one direction along the y-axis (Figure 6a). For example, the majority of fibres in sample A point towards the -90°. Similarly, fibres in sample C have a mean azimuth of -114°. By comparison, samples B and RM have much more azimuthal variation, though it should be remembered that samples B and RM have highly aligned fibres, and so these azimuthal leaning are slight. The two different azimuthal distributions seen could have been due to accidentally brushing individual tows or other human error during layup, displacement during infusion, or another manufacturing issue. However, the global position of each sample within the laminate is not known.

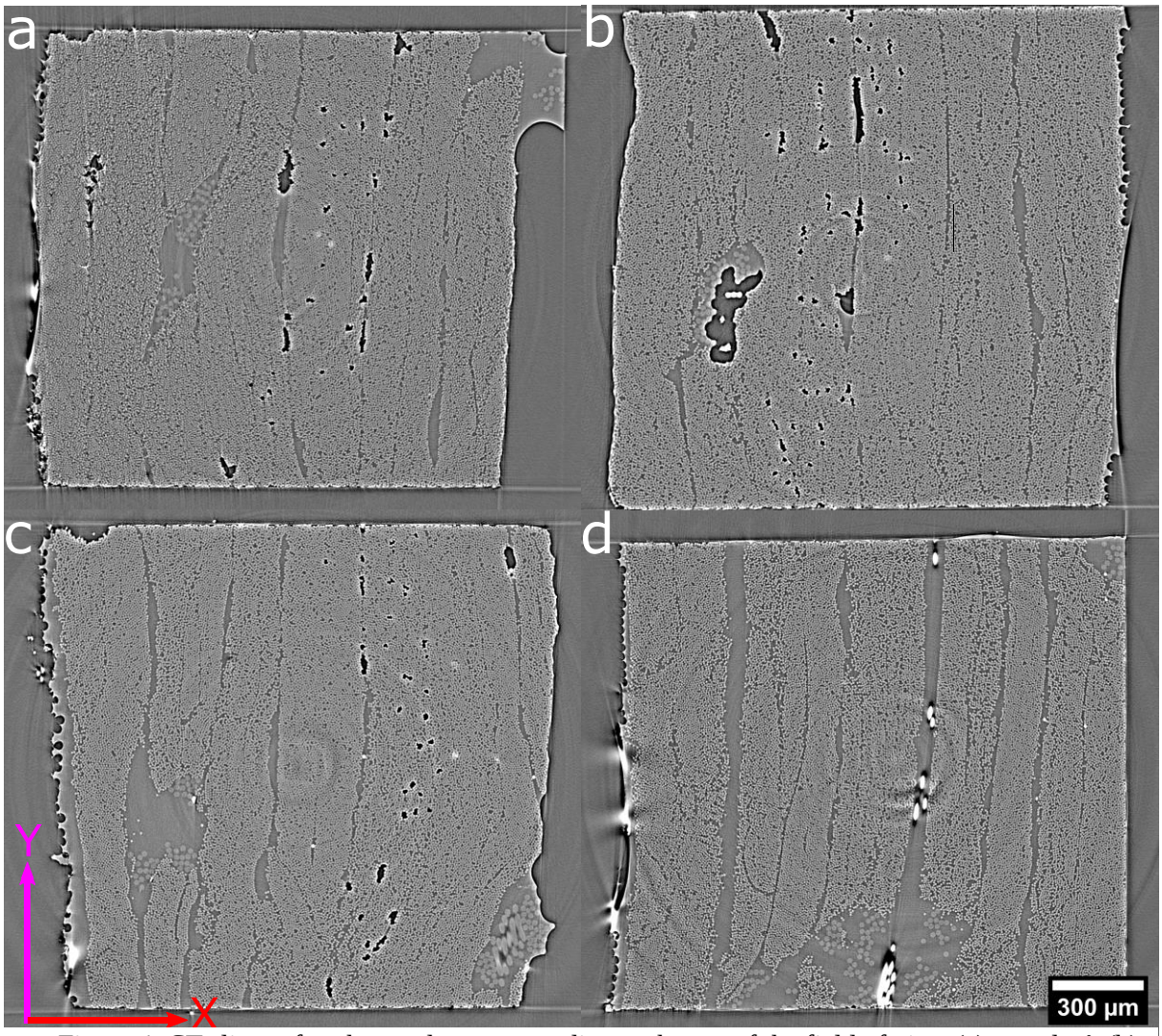

Figure 4: CT slices of each sample corresponding to the top of the field of view (a) sample A (b) sample B (c) sample C (d) RM sample

3.2 Relation Between Defect Distribution and Kinking Micromechanics

The kink plane orientation for each sample was determined from the post-mortem tomographs. A schematic showing the kink plane orientation is shown in Figure 8 (left), along with representative XY slices (middle) and central longitudinal slices taken parallel to the kink plane (right). Assessing the kink bands, the main differences are in the band width, ω, and geometry of multiple kink bands. The average band angles, β, of each sample all fall between 25° and 27°, and the average fibre rotation angle, φ, was between 64° and 72°. Key geometric parameters are labelled in Figure 8 (right). Samples A and C have quite large band widths, 369 and 366 µm, respectively, which remain relatively constant across the sample. Both samples, but especially sample A, also have a number of smaller kink bands within the main band (labelled 'sub-bands' in Figure 8 (right)). These smaller bands are at a similar fibre rotation angle to the main band but do not propagate across the entire sample width. Conversely, Sample B has a narrower bandwidth of 227 µm on average, and narrows to as low at 110 µm near the middle. There are multiple kink bands which span half the sample width and, rather than contained within a larger band, are in a 'stacked' geometry on top of one another. Similar to sample B, the band width of the RM sample is 90 µm on the left side of the sample, but broadens to 307 on the left side. The change is sudden, and occurs in the middle, where four stacked bands abruptly appear.

Two processes of band broadening have been reported in literature: band broadening with and without fibre fracture. The latter was first observed by Moran *et al* [12] and modelled by Budianksy [1].

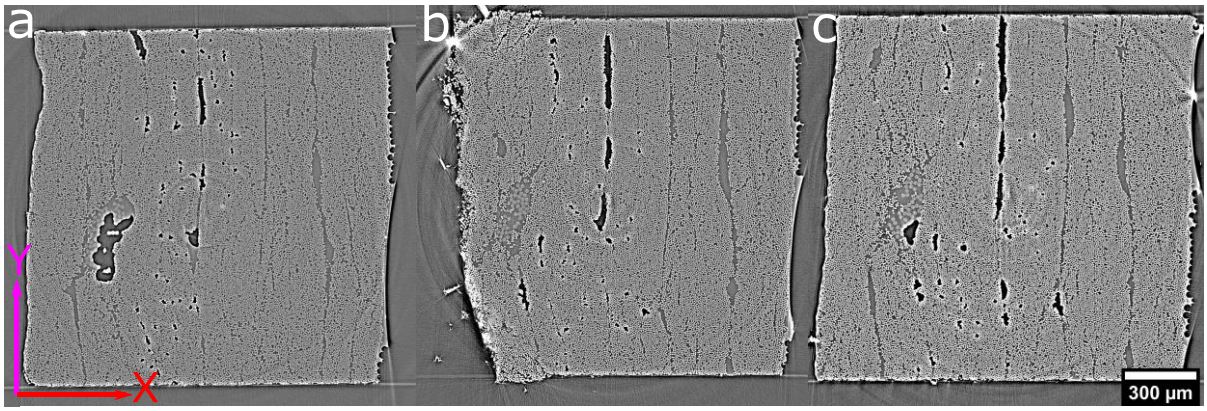

Figure 5: (a) top CT slice (b) middle slice (c) bottom slice for sample B

In this mode, steady state band broadening occurs after fibre lock-up causes the kinked region to extend laterally before fibre fracture delineates the second edge of the band. Band broadening with fibre fracture is more widely reported and occurs after a narrow kink band has formed fully. Then, with increased loading, excessive bending of the fibres adjacent to the kinked region cause the formation of subsequent 'stacked' bands [11], [13]. Overall the well-aligned samples have multiple stacked bands comprising a narrow kink band whereas the highly misaligned samples have wide band widths containing incomplete 'sub bands'. However, lacking clear *in situ* data for each sample, the possible relation between band width, band broadening mechanism, and initial fibre misalignment requires further investigation.

Regarding kink plane orientation, the sample geometry and notch placement were chosen to encourage kinking in the plane (XZ) perpendicular to the beam (Y-direction). However, it is immediately apparent from the XY slices Figure 8 (middle) that only the RM sample failed in this way, likely because this sample contained well aligned fibres, was minimally tortuous, with only one small void, and had resin rich regions well away from the initiation site. Conversely, Figure 8 (middle) indicates that sample A failed perpendicular to the expected kink plane, while sample B failed along the 45° direction, and sample C along -45°. Previous work [14] has suggested that the net misalignment may determine the kink plane. The fibres in sample A are, on average, leaning at -90° to the +X axis (see Figure 6a, Figure 7a). This may have initiated shear in the 90° plane rather than the intended 0° plane, suggesting a clear connection between original fibre orientation and the kink failure plane. Further, it does not appear that the resin rich regions or voids affected the propagation direction in this case, potentially because the voids and resin rich areas ran along the YZ planes in the sample, which would inhibit the kink propagation along the X axis.

In contrast, samples B and C both have propagation paths which appear to be correlated to a combination of fibre alignment and changes in local fibre volume fraction. The fibres in sample B had a mean zenith of only 1.4° and, while curved away from the notch (in the +X direction), the fibres were minimally tortuous. From Figure 7 b, the azimuth angle of the fibres in Sample B alternated between plies, and a

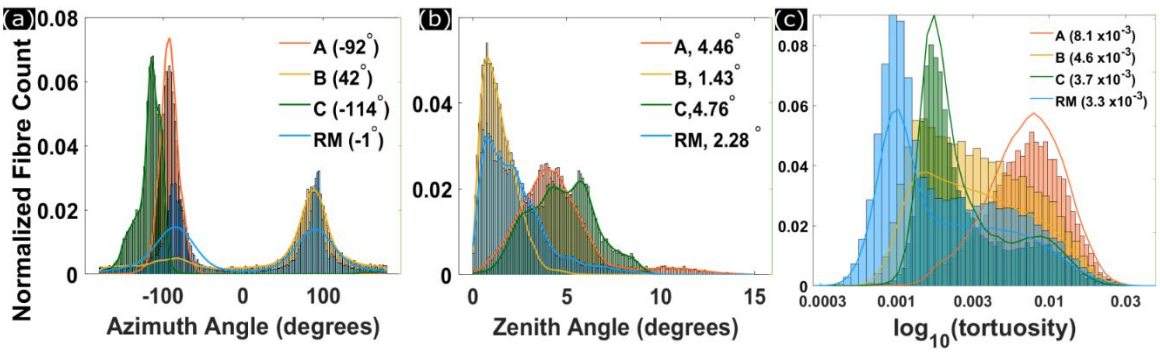

Figure 6: histograms for (a) azimuth (b) zenith and (c) tortuosity. Kernel distributions for each histogram are overlaid, and mean values are included in the legend entries.

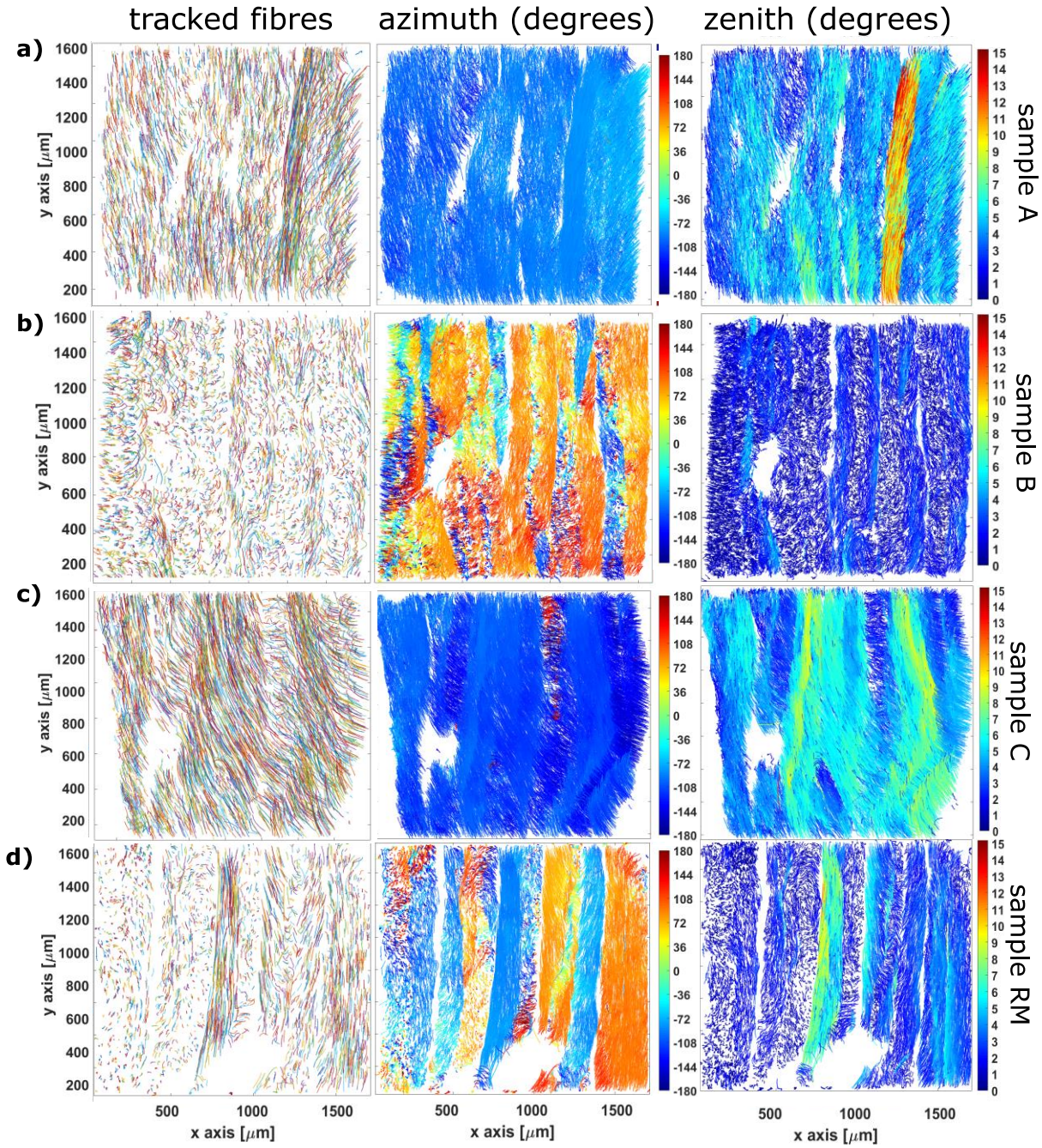

Figure 7: (Left column) A random 10% of tracked fibres projected onto XY axes. Fibres are coloured randomly. (Middle column) Colour maps of azimuthal distribution (in °). The + 90° and -90° directions correspond to +/- y-directions. (Right column) Colour maps of zenith distribution (in °). For clarity only 50% of the tracked fibres are included in the azimuth and zenith plots.

resin rich area spans majority of the Y axis located at x = 850 µm. From Figure 4, several voids are positioned along the Y axis in this resin-rich region, and large void is also present at (x,y) = (550 µm, 1000 µm). The kink initiated at the front of the sample, near the notch. Prior to failure, fibre buckling was observed during testing, likely enabled by the voids along x = 850 µm. From the CT slice in Figure 4, it is clear most of these voids are distributed in two-thirds of the sample volume, but not in the corner where failure initiated. In the corner of initiation, the fibre azimuth are evenly distributed between positive and negative 90°, so overall pointing in the positive X direction. The arrangement of voids and resulting narrow band (Figure 8b) suggest lateral (rather than longitudinal) shear could have occurred in the corner of initiation towards the buckled area along the 45° direction.

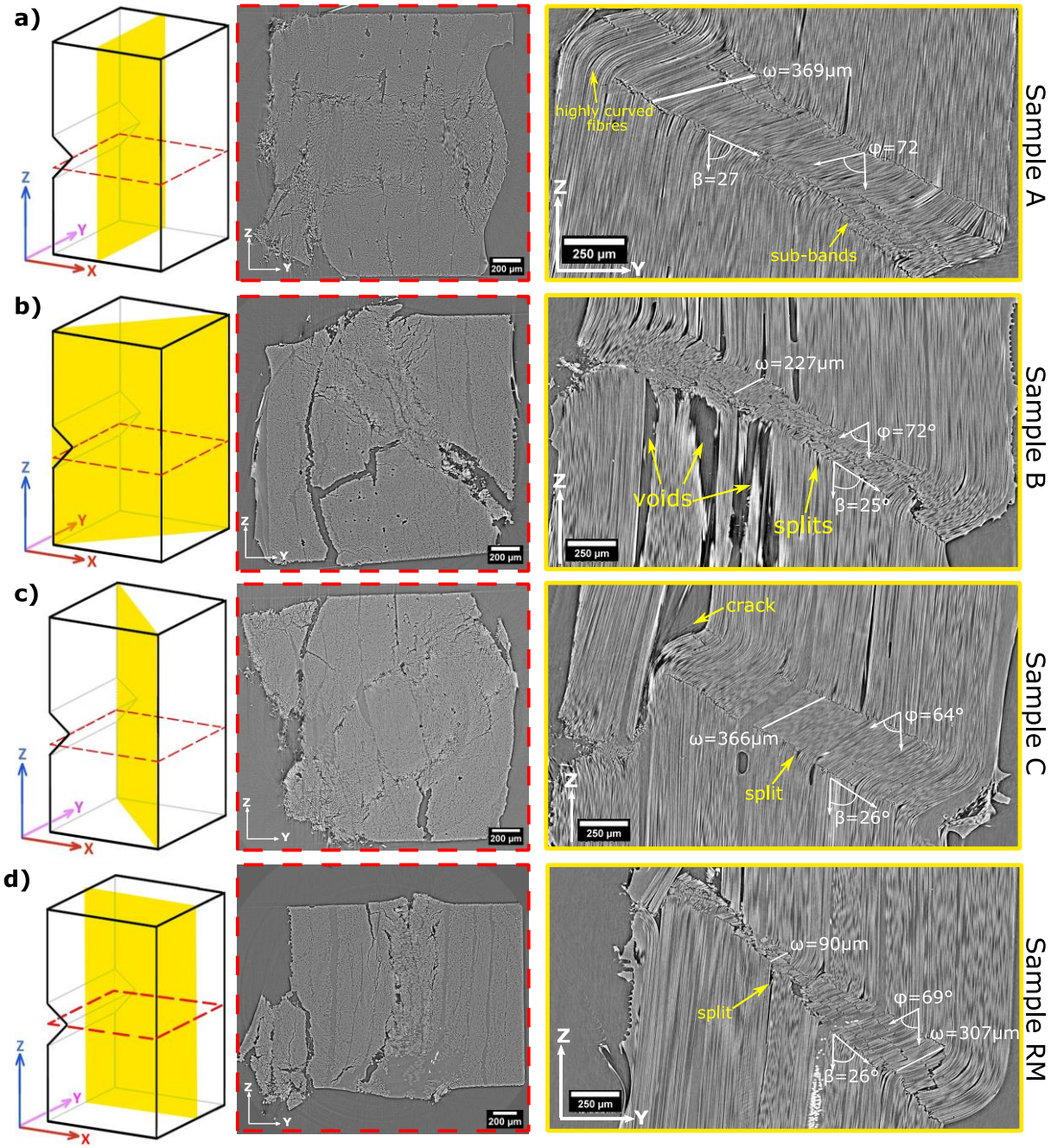

Figure 8: **(left column)** Schematic for each sample showing the central cross-sectional (XY) CT slice location (dashed red), and central longitudinal slice (yellow) parallel to the kink plane, **(middle column)** central XY CT slice **(right column)** central longitudinal slice. Examples of longitudinal splits vs pre-existing cracks and voids are highlighted.

The mean axial misorientation (zenith) of sample C was the most severe, at 4.8 ± 1.8°, and most of the fibres have an azimuth pointing in the -100° to -150° range. The fibres were curved towards the notch, but this sample was the least tortuous of the wavy samples. There was a large resin rich region centred at (x,y) = (500 μm, 600 μm) which coincided with a ply interface near x = 500 μm (Figure 7c). From the CT slice in Figure 4, voids were concentrated on the opposite side of the sample along one ply interface (roughly x = 1100). The kink band initiated at the back face of the sample, near the notch and away from the described defects. Potentially, the kink band would have propagated parallel to the misaligned fibres as in sample A if not for the resin rich area, forcing a net propagation direction of - 45°.

Similarly, the fibres with the most severe zenith angle are along the -45° direction as well, which may have encouraged propagation along this orientation.

Fibre misalignment angle seemed to be the most significant factor towards kink plane only in samples A and C, which are severely tilted in one direction and other defects did not impede or influence propagation. Clearly, however, it is not possible to separate the role of fibre misorientation from that of the voids and resin rich areas for these samples. Especially samples B, where failure seems driven by shearing due to voids, and in the RM sample, which was dominated by shear given no significant defects. Fibre undulation, quantified by tortuosity, did not seem as impactful for any sample, but, calculating tortuosity did enable identifying that the fibres were misaligned rather than an ambiguous combination of misaligned and wavy. Ultimately, further work is required to isolate the effect of fibre misorientation on kinking direction. Careful sample design remains one of the key limitations moving forward with similar micromechanical studies, and is further complicated by the requirement of miniscule samples to achieve high spatial resolution using CT. Potentially, using laminates made from pre-preg or with an autoclave would minimize local variations in fibre volume fraction. Finally, analyses presented were done manually for only four samples. Processing statistically significant CT data sets requires advances in automated data processing in 3D due to the huge file sizes and thousands of images associated with just a single tomograph.

4 CONCLUSIONS

High resolution CT scans (0.66 μm^3 per voxel) were recorded for four UD CFRP samples before and after axial compression; Samples A, B, and C were manufactured to be intentionally wavy, and a fourth baseline ‘RM’ sample had randomly misoriented straight fibres. The pre-test CT scans were used to resolve individual fibres and determine the severity of their misalignment (zenith angle), direction of misalignment (azimuth angle), and severity of waviness (tortuosity). The four samples each had a unique spatial distribution of defects and misorientation and failed in four different orientations. Postmortem scans were used to establish trends between kinking micromechanics and the spatial distribution of voids, resin rich areas, and fibre misorientation. The resulting kink planes were compared against the initial defects and misorientation to determine likely factors influencing the kink propagation direction.

In the case (RM) where fibres were minimally tortuous, well aligned fibres, and largely defect free failure was initiated by the notch and the kink plane, as expected. Fibres in sample A were most severely misaligned to the Z axis and had the least variation in azimuthal angle. The kink plane propagated parallel to the average azimuth of the misaligned fibres, strongly suggesting a correlation between the direction of fibre misalignment and kinking micromechanics.

For samples B and C, it appears that a combination of void location, resin rich regions, and fibre alignment contribute to the propagation direction. Although resin infusion was chosen to make samples with controlled undulation, this method resulted in high porosity, so it was not possible to separate the role of fibre misorientation from that of the voids and resin rich areas. Further, it is unclear what role the fibre curvature plays on compressive failure because the propagation was dominated by other defects, namely local fibre volume fraction and fibre misalignment. In summary, these results demonstrate how X-ray CT can help us better quantify the fibre orientations and thus better understand the effect of defects and fibre misorientation on the initiation and propagation direction of kink banding under compressive loading.

ACKNOWLEDGEMENTS

We would like to thank the European Synchrotron Research Facility (ESRF) for the beamtime. Thanks also go to Dr Vincent Maes for his time, insight, and thoughtful discussion. This work was also supported by an EPSRC International Centre to Centre grant with the ESRF (EP/W003333/1) and the NRF for Laboratory-based X-ray CT (NXCT), funded (EP/T02593X/1). NXCT is hosted within the Henry Royce Institute for Advanced Materials, established through EPSRC grants EP/R00661X/1, EP/P025498/1 and EP/P025021/1.

REFERENCES

[1] B. Budiansky, N.A. Fleck, J.C. Amazigos, "On Kink _Band Propagation In Fiber Composites", *J. Mech. Phys. Solids*, **46**, 1998, pp. 1637–1653,(doi: 10.1016/S0022-5096(97)00042-2.)

[2] B. Budiansky and N. A. Fleck, "Compressive failure of fibre composites," *J. Mech. Phys. Solids*, **41**, 1993, pp. 183–211, (doi: 10.1016/0022-5096(93)90068-Q.)

[3] N. A. Fleck, "Compressive Failure of Fibre Composites," *Adv. Appl. Mech.*, vol. **33**, Academic Press, 1997.

[4] B. Rosen W., "Mechanics of composite strengthening," presented at the Fibre Composite Materials, Ohio: American Society for Metals, 1965.

[5] S. Kyriakides, R. Arseculeratne, E. J. Perry, and K. M. Liechti, "On the compressive failure of fiber reinforced composites," *Int. J. Solids Struct.*, **32**, 1995, pp. 689–738, (doi: 10.1016/0020-7683(94)00157-R.)

[6] P. M. Jelf and N. A. Fleck, "Compression Failure Mechanisms in Unidirectional Composites". *J. Composite Materials*, **26**, 1992, pp. 2706-2726 (doi: 10.1177/00219983920260180)

[7] S. Pimenta, R. Gutkin, S. T. Pinho, and P. Robinson, "A micromechanical model for kink-band formation: Part I — Experimental study and numerical modelling," *Compos. Sci. Technol.*, **69**, 2009, pp. 948–955 (doi: 10.1016/j.compscitech.2009.02.010)

[8] R. Gutkin, S. T. Pinho, P. Robinson, and P. T. Curtis, "On the transition from shear-driven fibre compressive failure to fibre kinking in notched CFRP laminates under longitudinal compression," *Compos. Sci. Technol.*, **70**, 2010, pp. 1223–1231 (doi: 10.1016/j.compscitech.2010.03.010)

[9] Y. Wang, C. Soutis, and P. J. Withers, "X-Ray Microtomographic Imaging Of Kink Bands In Carbon Fibre-Epoxy Composites," *Proceedings of the 16TH European Conference On Composite Materials , ECCM16 2014, Seville, Spain, 22-26 June 2014*

[10] M. Ueda, K. Mimura, and T.-K. Jeong, "In situ observation of kink-band formation in a unidirectional carbon fiber reinforced plastic by X-ray computed tomography imaging," *Adv. Compos. Mater.*, **25**, 2016 pp. 31–43 (doi: 10.1080/09243046.2014.973173)

[11] M. P. F. Sutcliffe and N. A. Fleck, "Microbuckle propagation in carbon fibre-epoxy composites," *Acta Metall. Mater.*, **42**, 1994 pp. 2219–2231,1994 (doi: 10.1016/0956-7151(94)90301-8)

[12] P. M. Moran, X. H. Liu, and C. F. Shih, "Kink band formation and band broadening in fiber composites under compressive loading," *Acta Metall. Mater.*, **43**, 1995 pp. 2943–2958, doi: (10.1016/0956-7151(95)00001-C).

[13] J. Hapke, F. Gehrig, N. Huber, K. Schulte, and E. T. Lilleodden, "Compressive failure of UD-CFRP containing void defects: In situ SEM microanalysis," *Compos. Sci. Technol.*, **71**, 2011, pp. 1242–1249 (doi: 10.1016/j.compscitech.2011.04.009).

[14] Y. Wang *et al.*, "Evolution of fibre deflection leading to kink-band formation in unidirectional glass fibre/epoxy composite under axial compression," *Compos. Sci. Technol.*, **213**, 2021 p. 108929 (doi: 10.1016/j.compscitech.2021.108929).

[15] Y. Wang, S. C. Garcea, T. Lowe, E. Maire, C. Soutis, and P. J. Withers, "Ultra-Fast Time-Lapse Synchrotron Radiographic Imaging Of Compressive Failure In CFRP," *Proceedings of the 17th European Conference on Composite Materials ECCM17, Munich, Germany, 26-30th June 2016*

[16] K. Nelms ,Y. Wang, Y. Chen, A. Rack, S. Rawson, J. Adrien, E. Maire, P. Withers, "Effect Of Fiber Microstructure On Kinking In Unidirectional Carbon Fiber Reinforced Composites Imaged In Real Time Under Axial Compression," *Proceedings of the 20th European Conference on Composite Materials ECCM20, Lausanne, Switzerland, 26-30 June, 2022* pp. 279–286

[17] A. S. Argon, "Fracture of Composites," *Treatise on Materials Science & Technology*, **1**, 1972, pp. 79–114 (doi: 10.1016/B978-0-12-341801-2.50007-2).

[18] C. J. Creighton and T. W. Clyne, "The compressive strength of highly-aligned carbon-®bre/epoxy composites produced by pultrusion," *Compos. Sci. Technol.*, **60**, 2000, pp. 525-533 (doi:10.1016/S0266-3538(99)00153-0)

[19] I. Tretiak, L. Kawashita, and S. Hallett, "Effect Of Voids On Interlaminar Behaviour Of Carbon/Epoxy Composites," *Proceedings of the 17th European Conference on Composite Materials ECCM17 2016, Munich, Germany, 26-30th June 2016*

[20] I. Tretiak and R. A. Smith, "A parametric study of segmentation thresholds for X-ray CT porosity characterisation in composite materials," *Compos. Part Appl. Sci. Manuf.*, **123**, 2019 pp. 10–24 (doi: 10.1016/j.compositesa.2019.04.029).

[21] T. Takahashi *et al.*, "Unidirectional CFRP kinking under uniaxial compression modeled using synchrotron radiation computed tomography imaging," *Compos. Struct.*, **289**, 2022, p. 115458 (doi: 10.1016/j.compstruct.2022.115458).

[22] S. W. Yurgartis, "Measurement of small angle fiber misalignments in continuous fiber composites," *Compos. Sci. Technol.*, **30**, 1987, pp. 279–293 (doi: 10.1016/0266-3538(87)90016-9).

[23] F. B. Salling, N. Jeppesen, M. R. Sonne, J. H. Hattel, and L. P. Mikkelsen, "Individual fibre inclination segmentation from X-ray computed tomography using principal component analysis," *J. Compos. Mater.*, **56**, 2022, pp. 83–98,(doi: 10.1177/00219983211052741).

[24] C. J. Creighton, M. P. F. Sutcliffe, and T. W. Clyne, "A multiple field image analysis procedure for characterisation of fibre alignment in composites," *Compos. Part Appl. Sci. Manuf.*, **32**, 2001, pp. 221–229,(doi: 10.1016/S1359-835X(00)00115-9).

[25] D. Wilhelmsson and L. E. Asp, "A high resolution method for characterisation of fibre misalignment angles in composites," *Compos. Sci. Technol.*, **165**, 2018, pp. 214–221 (doi: 10.1016/j.compscitech.2018.07.002).

[26] K. Kratmann, M. Sutcliffe, L. Lilleheden, R. Pyrz, and O. Thomsen, "A novel image analysis procedure for measuring fibre misalignment in unidirectional fibre composites," *Compos. Sci. Technol.*, **69**, 2009, pp. 228–238, (doi: 10.1016/j.compscitech.2008.10.020).

[27] P. J. Withers *et al.*, "X-ray computed tomography," *Nat. Rev. Methods Primer*, **1**, 2021, p. 18, (doi: 10.1038/s43586-021-00015-4).

[28] S. C. Garcea, Y. Wang, and P. J. Withers, "X-ray computed tomography of polymer composites," *Compos. Sci. Technol.*, **156,** 2018, pp. 305–319,(doi: 10.1016/j.compscitech.2017.10.023).

[29] G. Requena, G. Fiedler, B. Seiser, P. Degischer, M. Di Michiel, and T. Buslaps, "3D-Quantification of the distribution of continuous fibres in unidirectionally reinforced composites," *Compos. Part Appl. Sci. Manuf.*, **40**, 2009, pp. 152–163,(doi: 10.1016/j.compositesa.2008.10.014).

[30] S. Gomarasca, D. M. J. Peeters, B. Atli-Veltin, and C. Dransfeld, "Characterising microstructural organisation in unidirectional composites," *Compos. Sci. Technol.*, **215**, 2021, p. 109030 (10.1016/j.compscitech.2021.109030).

[31] S. Morita, M. Ueda, T. Takahashi, K. Kajiwara, A. Yoshimura, and N. Sugiura, "Performance assessment for fiber tracking of unidirectional carbon fiber reinforced plastic by digital image correlation of X-ray computed-tomography," *Adv. Compos. Mater.*, **32**, 2023, pp. 35–47 (doi: 10.1080/09243046.2022.2071117).

[32] M. J. Emerson, A. B. Dahl, K. Conradsen, and V. A. Dahl, "Insegt Fibre: A User-Friendly Software For Individual Fibre Segmentation", *In Proceedings of 22nd International Conference on Composites Materials ICCM22 2019, Melbourne, Australia, 11-16 August 2019.*

[33] T. Weitkamp, P. Tafforeau; E. Boller, P. Cloetens; JP. Valade; P. Bernard, F. Peyrin; W. Ludwig; L. Helfen; J. Baruchel., "Status and evolution of the ESRF beamline ID19," *AIP Conf. Proc.*, **1221**, 2010, pp. 33–38, (doi: 10.1063/1.3399253).

[34] H. Payno, P. Paleo, C. Nemoz, P. Cloetens, M. di Michiel, A. Rack, P. Tafforeau, V.A. Solé and N.R. Viganò., "Overcoming the data processing challenges of unifying tomography techniques at ESRF," *J. Phys. Conf. Ser.*, **2380**, 2022 p. 012106 (doi: 10.1088/1742-6596/2380/1/012106).

[35] D. Paganin, S. C. Mayo, T. E. Gureyev, P. R. Miller, and S. W. Wilkins, "Simultaneous phase and amplitude extraction from a single defocused image of a homogeneous object," *J. Microsc.*, **206**, 2002, pp. 33–40 (doi: 10.1046/j.1365-2818.2002.01010.x).

[36] M. Beister, D. Kolditz, and W. A. Kalender, "Iterative reconstruction methods in X-ray CT," *Phys. Medica*, **28**, pp. 94–108, Apr. 2012, (doi: 10.1016/j.ejmp.2012.01.003).

[37] I. T. Jolliffe, "Mathematical and Statistical Properties of Population Principal Components," *Principal Component Analysis*, New York, NY: Springer, 2002, pp. 10–28 (doi: 10.1007/0-387-22440-8_2).